Crossref
DOI: 10.31643/2028/6445.33
Metallurgy and Metallurgical Engineering

Image-Based FEM Modeling of the Stress State in Hypereutectic High-Chromium Cast Irons

[1]Perezhogin V.Yu., [1]Panichkin A.V., [2]Małgorzata R.G., [1*]Abyl S.S.

[1] Institute of Metallurgy and Ore Beneficiation JSC, Satbayev University, Almaty, Kazakhstan
[2]Wroclaw University of Science and Technology, Wroclaw, Poland

** Corresponding author email: Abyl.S@stud.satbayev.university*

Received: *June 17, 2026*
Peer-reviewed: *July 26, 2026*
Accepted: *September 8, 2026*

ABSTRACT
We developed an approach to analyze local thermal stresses in hypereutectic high-chromium cast irons using image-based finite element modeling (FEM) based on real metallographic images. Model preparation included Otsu thresholding of the microstructure, filtering noise objects, and directly assigning the spatial phase distribution from the binarized image without intermediate geometry construction in computer-aided design (CAD) systems. To verify the proposed approach, Drawing Exchange Format (DXF)-based and image-based FEM models constructed from the same microstructural data were compared, and the influence of finite element size on the calculated stress state was investigated. The results showed that, with a progressive reduction in finite element size, the image-based simulation results approached those obtained using the DXF-based models despite the discrete pixel-based representation of the phase boundaries. The image-based approach reproduces the main features of the local stress distributions obtained using the DXF-based models while eliminating the need for image vectorization and intermediate CAD/DXF geometry construction, thereby substantially simplifying the preparation of computational models of real microstructures. The obtained results confirm the applicability of image-based FEM for comparative analysis of local thermal stress distributions in complex multiphase microstructures of high-chromium cast irons.

Keywords: hypereutectic high-chromium cast iron, image-based FEM, thermal stresses, M_7C_3 carbides, microstructure analysis, finite element modeling.

Information about authors:

Perezhogin Vitaliy Yurievich
PhD, Researcher, Materials Science Laboratory, Institute of Metallurgy and Ore Beneficiation JSC, Satbayev University, 050010, Shevchenko str., 29/133, Almaty, Kazakhstan. E-mail: v.perezhogin@satbayev.university; ORCID ID: https://orcid.org/0009-0006-7881-4786

Panichkin Alexander Vladimirovich
Candidate of Technical Sciences, Leading Researcher at the Materials Science Laboratory, Institute of Metallurgy and Ore Beneficiation JSC, Satbayev University, 050010, Shevchenko str., 29/133, Almaty, Kazakhstan. Email: a.panichkin@satbayev.university; ORCID ID: https://orcid.org/0000-0002-2403-8949

Małgorzata Rutkowska-Gorczyca
PhD, Habilitated Doctor of Engineering, Department of Mechanics, Wroclaw University of Science and Technology, 50-370 Wroclaw, Poland. E-mail: Malgorzata.Rutkowska-Gorczyca@pwr.wroc.pl; ORCID ID: https://orcid.org/0000-0003-2712-5914

Abyl Salima Serikkyzy
Doctoral student, Junior Researcher, Materials Science Laboratory, Institute of Metallurgy and Ore Beneficiation JSC, Satbayev University, 050010, Shevchenko str., 29/133, Almaty, Kazakhstan. E-mail: Abyl.S@stud.satbayev.university; ORCID ID: https://orcid.org/0009-0006-1904-3483

Introduction

Hypereutectic high-chromium cast irons are widely used under severe abrasive wear conditions due to their high hardness and significant content of the M_7C_3 ($(Fe, Cr)_7 C_3$) carbide phase [[1], [2], [3], [4], [5], [6]]. The performance of these materials is largely determined by the size and volume fraction of primary and eutectic carbides, their morphology, distribution within the austenitic matrix, and the characteristics of the phase boundaries [[7], [8], [9], [10]].

The presence of extended and branched carbide structures can lead to local stress concentrations and significantly affect crack initiation and fracture processes [[2], [11], [12]]. The local stress state in the carbide-matrix system has a significant influence on fracture resistance, wear resistance, and the likelihood of carbide-phase fracture during the service of high-chromium cast irons under thermal cycling and mechanical loading conditions.

Finite element modeling (FEM) methods are widely used to analyze local stress states in multiphase materials. One of the traditional approaches to constructing computational models of real microstructures involves vectorization of metallographic images followed by the generation of CAD/DXF geometry [[13], [14]]. However, when applied to complex real microstructures, this approach is characterized by labor-intensive model preparation, difficulties in finite element mesh generation, and the need for additional geometry processing. Furthermore, geometry simplification may result in the loss of specific features of the actual phase morphology.

An alternative approach is image-based FEM, which is based on the direct use of binarized metallographic images for constructing computational models [[13], [14], [15]]. This approach enables the actual geometry and spatial distribution of phases to be represented without intermediate CAD/DXF geometry construction, thereby substantially simplifying the preparation of finite element models of complex microstructures.

FEM methods are widely applied to the analysis of residual stresses in additive manufacturing and heterogeneous materials [[16], [17]]; however, their application to the microstructure-based analysis of multiphase alloys remains comparatively limited. Therefore, it is of interest to assess the feasibility of directly using binarized metallographic images for finite element modeling of such structures and to compare the resulting predictions with those obtained using the traditional DXF-based approach.

The aim of this study was to develop and verify an image-based FEM approach for analyzing the local distribution of thermal stresses in real microstructures of hypereutectic high-chromium cast irons by comparison with DXF-based modeling and by evaluating the influence of finite element discretization on the simulation results.

Materials and Methods

A hypereutectic high-chromium cast iron containing the M_7C_3 carbide phase was used as the material investigated in this study. The specimen used for the development of the methodology was melted in a UIFV-0.005 vacuum induction melting furnace. The charge consisted of a Ø50 mm bar of 50Kh steel in accordance with GOST 4543-2016 and high-carbon ferrochromium FeCr60C90Si2 in accordance with GOST 4757-91. The required carbon content was achieved by adding graphite powder with a particle size of 0.5-1 mm to the charge. Melting was carried out at a residual pressure of 50-70 Pa. The melt temperature was monitored using a stationary spectral-ratio infrared pyrometer, Termoskop-800-2S-VT1. After the melt surface reached a temperature of 1500 °C, the inductor current was reduced to prevent further overheating, and the melt was held for 20 min. Air was then admitted into the furnace, the vacuum chamber lid was moved aside, and the melt was poured into a mold (Figure 1) made of PKhKTs-20-grade periclase-chromite bricks.

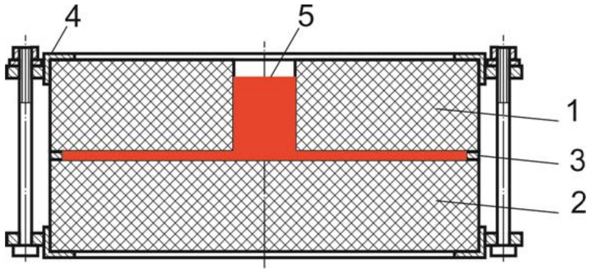

Figure 1 – Casting mold (1 – upper plate, 2 – lower plate, 3 – steel frame, 4 – mold clamping fixture, 5 – casting)

The resulting casting was a plate with a thickness of 6 ± 0.5 mm and dimensions of 100×350 mm, with a sprue located at its center. A 100×29 mm plate was cut from the resulting casting by wire electrical discharge machining using a DK7720 machine. The specimen was not subjected to any heat treatment. One surface of the plate was then leveled by electrical discharge machining by removing a thin layer up to 0.7 mm thick. The actual alloy composition was determined by semiquantitative X-ray fluorescence analysis and quantitative carbon analysis (Table 1).

Table 1 - Actual chemical composition of the alloy

Element	Fe	Cr	C	Mn	Ni	Mo
wt.%	70.17	24.3	4.48	0.72	0.17	0.16

Table 2 - Fraction and dimensional characteristics of the carbide phase in the investigated alloy

Structure parameter	Measurement result
Carbide fraction, %	25.6
Primary carbide fraction, %	16.5
Average length of primary carbides in the cross-sectional plane, μm	32.9
Average thickness of primary carbides in the cross-sectional plane, μm	15.8
Average area of primary carbides, μm^2	312

The prepared surface was ground using SiC abrasive paper and polished using diamond pastes. The microstructure was revealed by rubbing the polished surface with a cotton swab soaked in an etchant containing 100 mL HCl, 7 mL H_2SO_4, and 30 g $CuSO_4$. Metallographic images were acquired using a Leica DM IRM metallographic workstation. Microstructural analysis was performed using images obtained by optical microscopy. Image processing was carried out using ImageJ/Fiji software [18]. The total carbide fraction, primary carbide fraction, and dimensional characteristics of the primary carbides are presented in Table 2.

Image preparation included conversion of the metallographic images to 8-bit grayscale, Otsu thresholding [19], and subsequent filtering of the binarized images to identify the carbide phase [20]. A distinction should be made between the preliminary removal of noise objects with an area of less than 4 px^2, which was performed for all images, and the subsequent structural filtering of carbide objects by area, which was used to generate one of the investigated microstructural variants. Filtering was performed using the standard Analyze Particles tools available in ImageJ/Fiji. The threshold value of 4 px^2 corresponded to a minimum object size of 2×2 pixels. Objects with smaller areas were regarded as binarization noise artifacts because their dimensions were substantially smaller than the characteristic dimensions of the carbide inclusions. For the DXF-based models, objects intersecting the image boundaries were additionally removed because they resulted in open contours during CAD geometry construction. This step was not required for image-based FEM because the phase distribution was assigned directly from the binarized image.

According to thermodynamic calculations for the Fe-Cr-C system [[21], [22]] and experimental studies [[3], [9], [23]], the predominant carbide phase in hypereutectic high-chromium cast irons within the investigated composition range is M_7C_3, with Cr and Fe being the predominant elements in its metallic sublattice. Accordingly, the finite element model of the microstructure was considered as a two-phase system consisting of an austenitic matrix and an M_7C_3 carbide phase. This representation is a modeling approximation because the composition of M_7C_3 carbides in real high-chromium cast irons may vary due to differences in the Fe-to-Cr ratio in the metallic sublattice; consequently, their thermophysical and mechanical properties may also differ from those of pure Cr_7C_3. In the present study, the properties of Cr_7C_3 were therefore used as effective parameters for the M_7C_3 carbide phase. Accordingly, the calculated stress values should primarily be interpreted comparatively, for analyzing the characteristics of stress distribution and localization within the real microstructure, rather than as exact absolute stress values for a specific alloy.

Constant thermophysical and mechanical properties of the austenitic matrix and the M_7C_3 carbide phase were used for finite element modeling. Austenitic stainless steel 316L (1.4435, X2CrNiMo18-12) was selected as the model material for the austenitic matrix and was used as an effective approximation of the properties of the austenitic metallic matrix of high-chromium cast iron rather than as its exact chemical analogue. The matrix properties were selected taking into account published data for 316L steel [24]. The properties of the Cr_7C_3 carbide phase were selected based on published experimental and computational data for carbides of this type [[25], [26]]. The thermophysical and mechanical properties used in the calculations are presented in Table 3.

Table 3 - Thermophysical and mechanical properties of the carbide phase and austenitic matrix

Property	**Value**		***Unit***
	Austenite	***Cr_7C_3 carbide***	
Coefficient of thermal expansion	1.7e-5	1e-5	1/K
Thermal conductivity	20	16	W/(m·K)
Density	8e3	7e3	kg/m³
Young's modulus	200e9	310e9	Pa
Poisson's ratio	0.30	0.23	-

Finite element modeling was performed in COMSOL Multiphysics using a two-dimensional steady-state thermomechanical formulation. The plane strain approximation was adopted for the mechanical problem. The thermal problem was defined using the Heat Transfer in Solids interface, while the stress-strain state was modeled using the Solid Mechanics interface. The thermal and mechanical problems were coupled through the Thermal Expansion multiphysics interface. The calculations were performed using a thermal strain reference temperature of T_{ref} = 1420.15 K and a final temperature of T = 293.15 K, corresponding to a temperature decrease of 1127 K. In this formulation, the kinetics of the cooling process and the spatial and temporal evolution of the temperature field were not modeled. To prevent rigid-body motion of the computational domain, kinematic constraints were applied at two lower corner points of the square computational domain. At the lower-left corner, displacements were constrained in both directions (u_x=0, u_y=0), whereas at the lower-right corner, only the vertical displacement was constrained (u_y=0), leaving the horizontal displacement free. This constraint scheme eliminated translational and rotational rigid-body motion of the computational domain without rigidly fixing its external boundaries.

To evaluate the influence of spatial discretization, calculations were performed using different levels of finite element mesh refinement. At the initial stage, the standard COMSOL Multiphysics mesh refinement levels were used, after which the element size was specified using user-defined mesh parameters. The maximum finite element size was progressively reduced to evaluate the sensitivity of the calculated stress state to spatial discretization and to select rational mesh parameters.

The calculations were performed using a stationary solver in a Fully Coupled formulation. A Direct solver was used to solve the linear system of equations, while the nonlinear iterations were performed using Newton's method with automatic parameter selection.

The DXF-based FEM models were generated by vectorizing the preprocessed binarized images in Inkscape using the standard tracing parameters. The resulting vector contours were saved in DXF format and imported into COMSOL Multiphysics [27] to construct the geometry of the computational domain and subsequently generate the finite element mesh. Thus, the DXF-based approach included an intermediate step in which the raster image was converted into vector geometry. This approach provided explicit phase boundaries and enabled the construction of topologically consistent FEM models based on the real microstructure.

The image-based FEM models were constructed directly from the preprocessed binarized images without intermediate vectorization or CAD/DXF geometry construction [[13], [14], [15]]. The binarized image was imported directly into COMSOL Multiphysics [27] using the built-in Image function. Pixel values were used to define the spatial distribution of the properties of the matrix and M_7C_3 carbide phase within a single two-dimensional computational domain. The finite element mesh was generated directly over the computational domain. The image-based FEM approach was implemented entirely using the built-in capabilities of COMSOL Multiphysics and did not require additional programming scripts or external automation tools.

The stress state was analyzed using the distributions of the first and second principal stresses, SP1 and SP2. SP2 maps were used to visualize the localization of compressive stresses in the model and real microstructures, whereas quantitative comparison between the DXF-based and image-based models was performed using SP1 as a measure of local tensile stresses, which are of primary interest with respect to potential microcrack initiation. For quantitative comparison, the mean SP1 value and the 95th percentile (P95) of SP1 were determined. The use of P95 reduced the influence of isolated local extrema associated with the geometry of the phase boundaries and finite element mesh discretization.

The developed model was primarily intended for comparative analysis of the effects of the microstructure representation method, finite element discretization parameters, and carbide-phase morphology on the distribution of local thermal stresses. Because constant phase properties and a stationary formulation were used, the calculated stress values were not interpreted as exact absolute values of residual stresses in the real material.

Results and Discussion

For a preliminary assessment of the influence of carbide-phase morphology and for the development of the FEM approach, model carbide structures of different shapes were used (Figure 2). These models were used to analyze the local distribution of thermal stresses and to evaluate the influence of carbide-phase geometry on the formation of stress concentrations [[2], [11]].

The obtained results showed the formation of localized regions of elevated stress near sharp-angled regions of the carbide phase and in areas with complex phase-boundary geometry [28]. This confirms the significant influence of carbide morphology on the local stress state and supports the need to analyze real microstructures without additional geometric idealization.

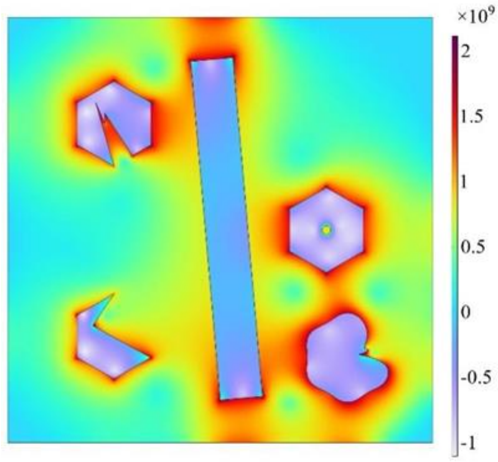

Figure 2 – Distribution of the second principal stress SP2 (Pa) for model carbide structures with complex geometries

The formation of local stress concentrations is associated with differences in the thermophysical and mechanical properties of the M_7C_3 carbide phase and the austenitic matrix, primarily their coefficients of thermal expansion and elastic properties [[3], [11], [12]]. The difference in the coefficients of thermal expansion results in different thermal strains of the phases under the imposed temperature change and, due to strain compatibility at the phase boundary, leads to the formation of local stress concentrations. The most pronounced stress localization occurs near sharp-angled, elongated, and geometrically complex regions of the carbide phase [[2], [11]].

Local tensile stresses in the carbide phase may contribute to microcrack initiation and subsequent carbide fracture during both the production and service of high-chromium cast iron components. Therefore, analysis of the stress distribution in the carbide - matrix system is of practical interest for assessing the potential fracture resistance and performance of this class of materials.

Following the analysis of the model structures, the developed approach was applied to real metallographic images of hypereutectic high-chromium cast irons (Figure 3).

To evaluate the influence of preliminary microstructural image processing on the FEM simulation results, different representations of the carbide structure were considered. At the first stage, objects were filtered by area. At an image scale of 50 µm = 839 px, the threshold area of 7701 px^2 corresponded to approximately 27.35 $µm^2$; objects with smaller areas were removed from the binarized image. The threshold value was selected based on a characteristic change in the object area distribution that separated numerous small microstructural constituents from a group of larger carbide objects (Figure 4a).

In addition, morphological filtering of the remaining objects was performed using the parameter P^2/S, where P is the object perimeter, and S is its area. This dimensionless parameter was used to quantitatively characterize contour complexity and branching. A threshold value of 207.05 was adopted; objects with higher parameter values, characterized by more complex and branched morphologies, were removed, whereas more compact objects were retained (Figure 4b).

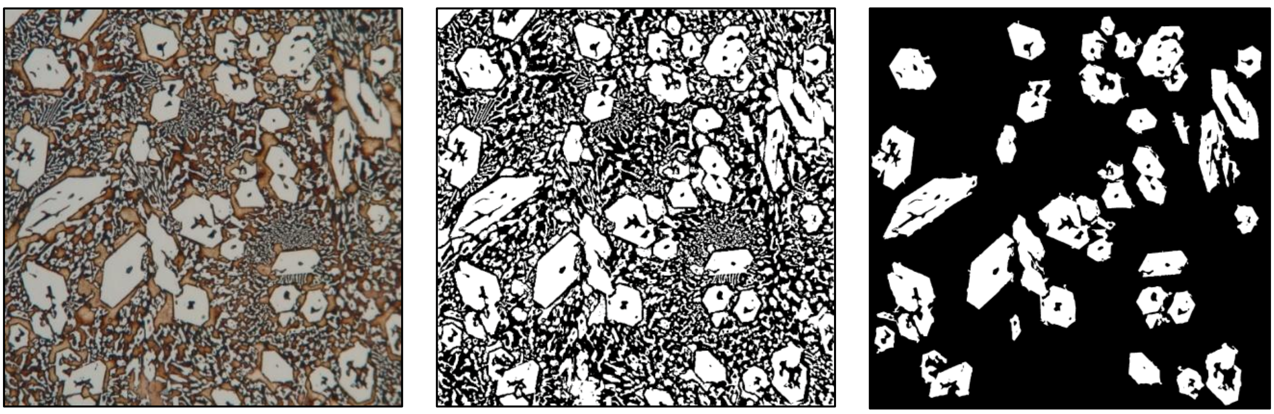

a b c

Figure 3 – Image processing stages (×750) a – original image; b – Otsu thresholding; c – idealized representation of primary carbide morphology

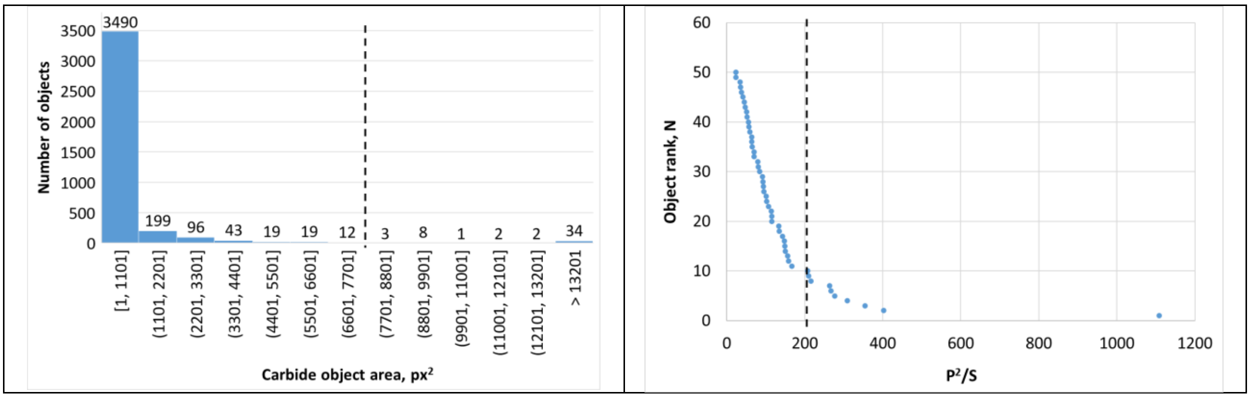

Figure 4 – Criteria for filtering carbide objects during preprocessing of the binarized image
a – distribution of carbide objects by area; b – morphological parameter P^2/S as a function of object number

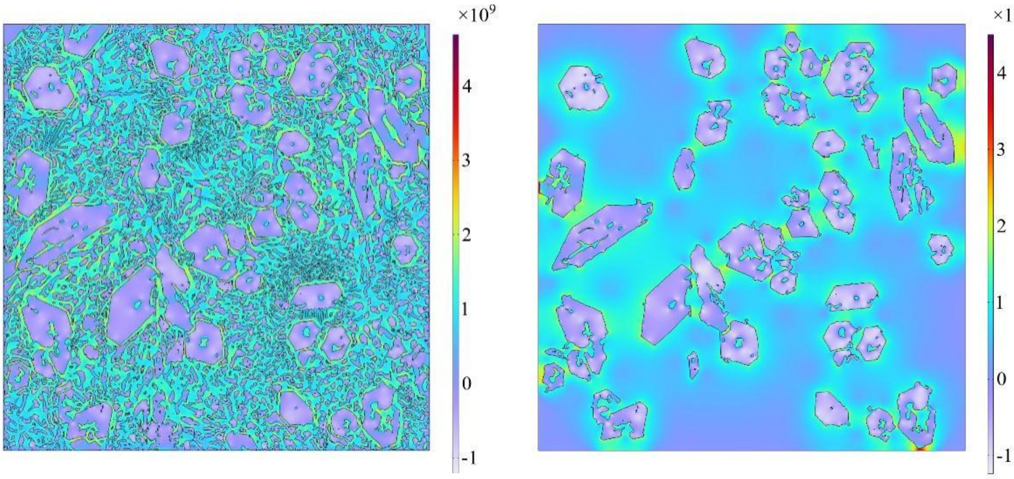

a b

Figure 5 – Distribution of the second principal stress SP2 (Pa) in DXF-based FEM models of the real microstructure: a – model based on the complete binarized image;
b – model based on the idealized representation of primary carbides

For quantitative comparison of the DXF-based and image-based FEM models, five microstructure representations were used: 1 – idealized representation of primary carbide morphology; 2 – image after morphological filtering using the P^2/S parameter; 3 – image after filtering carbide objects by area; 4 – image after removing objects intersecting the boundaries of the analyzed region; and 5 – complete binarized image after removal of only small noise objects with areas below 4 px^2. The same image variants were used to construct both the DXF-based and image-based FEM models, enabling direct comparison of the two approaches using identical representations of the initial microstructure.

The DXF-based FEM simulation of the real microstructure showed that the maximum stresses were localized predominantly near the phase boundaries, particularly near sharp-angled regions of the carbide phase (Figure 5). The obtained results confirmed the significant influence of carbide morphology on the distribution of local stresses. This stress distribution pattern is consistent with the established understanding of strain localization in systems containing rigid carbide inclusions [[2], [11], [12]].

Comparison of the complete binarized microstructure with its idealized representation showed that the removal of part of the carbide network changes the local stress distribution pattern. This indicates the importance of preserving the actual morphology of both primary and eutectic carbides when analyzing the local stress state.

Despite its ability to explicitly represent phase boundaries, the DXF-based approach was characterized by labor-intensive model preparation. Vectorization of binarized images, generation of CAD/DXF geometry, and subsequent finite element mesh generation became increasingly difficult as the geometric complexity of the carbide network increased. Therefore, further work focused on the development of an image-based FEM approach that enables calculations to be performed directly from binarized microstructural images without intermediate CAD geometry construction.

In the image-based FEM models, the phase distribution was defined directly from the binary image map. Unlike the DXF-based approach, this method did not require vectorization of phase boundaries or the construction of separate geometric domains for the carbide phase and the matrix. However, the discrete pixel-based representation of the phase boundaries necessitates an assessment of the influence of finite element size on the representation of the local stress state.

To evaluate the influence of finite element discretization, calculations were performed with a progressive reduction in the maximum finite element size. Reducing the maximum finite element size resulted in a more detailed representation of the phase-boundary geometry and local stress distribution and led to a gradual convergence of the image-based model results toward those obtained using the DXF-based representation (Figure 6). As part of the mesh sensitivity analysis, the maximum element size was progressively reduced to 0.2 µm; representative stages of this refinement are shown in the figure. Further mesh refinement, however, was accompanied by a substantial increase in computational cost.

Based on the results of the mesh sensitivity analysis, a maximum finite element size of 0.5 µm was selected for subsequent calculations, providing a reasonable balance between the level of detail in the calculated stress state and computational cost.

When larger mesh sizes were used, local stress maxima were smoothed due to insufficient representation of the complex phase-boundary geometry. Reducing the maximum finite element size enabled a more accurate representation of the local features of the stress distribution near the carbide phase and provided better agreement with the DXF-based modeling results [[13], [14], [15]].

For quantitative verification of the image-based FEM approach, the results of DXF-based and image-based simulations were compared for the five investigated microstructure representations (1-5), corresponding to different preprocessing variants. Maximum finite element sizes of 0.2 and 0.5 µm were used for the image-based models. For quantitative comparison, the mean SP1 value and the 95th percentile (P95) of SP1 in the M_7C_3 carbide phase were determined (Figure 7).

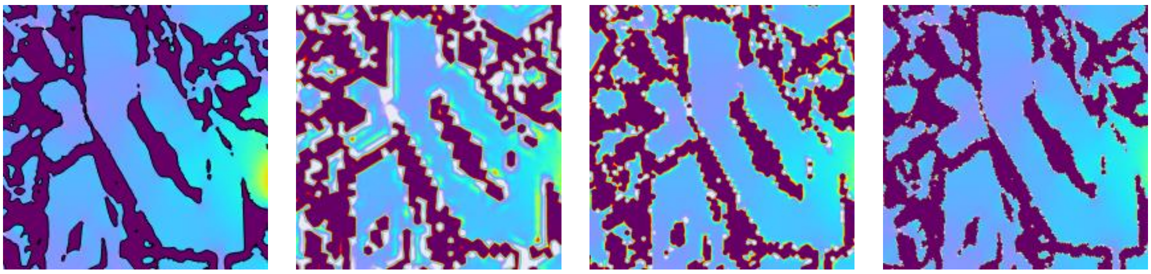

a b c d

Figure 6 – Comparison of SP1 stress fields for different models: a – DXF-based model; b – image-based model, mesh size 1.65 µm; c – image-based model, mesh size 0.5 µm; d – image-based model, mesh size 0.2 µm

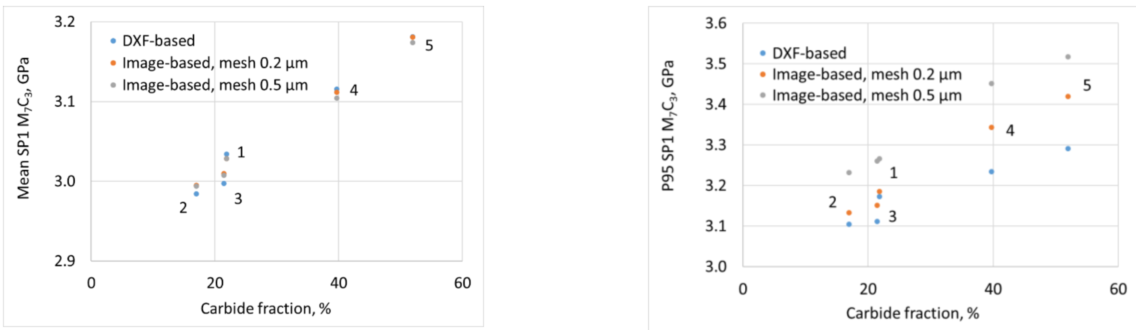

a b

Figure 7 – Comparison of stress-state characteristics in M_7C_3 carbides for the DXF-based and image-based FEM models a – mean SP1; b – P95 SP1

The obtained results show that the mean SP1 values in the M_7C_3 carbide phase calculated using the DXF-based and image-based FEM models are in good agreement for all investigated microstructure representations (Figure 7a). Reducing the maximum finite element size in the image-based model from 0.5 to 0.2 μm has only a minor effect on the mean SP1 values, indicating their relatively low sensitivity to further finite element mesh refinement.

More pronounced differences are observed for the P95 SP1 values (Figure 7b). Overall, at a maximum finite element size of 0.5 μm, the P95 values show greater deviations from the corresponding values obtained using the DXF-based model, particularly for the variants with a higher carbide-phase fraction. Reducing the maximum element size to 0.2 μm results in closer agreement in most of the investigated variants. This indicates a higher sensitivity of the upper part of the local stress distribution to spatial discretization and to the accuracy with which the complex phase-boundary geometry is represented.

Thus, the finite element size has a substantially smaller influence on the integral characteristics of the stress state represented by the mean SP1 values than on the characteristics of the upper part of the stress distribution. A mesh with a maximum element size of 0.5 μm provides stable representation of the mean stress characteristics at substantially lower computational cost, whereas further mesh refinement to 0.2 μm improves the representation of high local stress values.

Some differences between the models are associated with the different representations of the phase boundaries. The DXF-based model uses smoothed vector contours, whereas in image-based FEM the phase boundaries are represented by the discrete pixel structure of the image.

Despite the differences in phase-boundary representation, the image-based FEM approach provides results comparable to those obtained using DXF-based modeling and enables calculations to be performed directly from binarized microstructural images without intermediate CAD geometry construction. The obtained results confirm the applicability of image-based FEM for comparative analysis of the stress state in high-chromium cast irons with different representations and morphologies of the carbide phase.

It should be noted that constant thermophysical and mechanical properties of the phases were used in the present study, without accounting for their temperature dependence, plastic deformation, or possible phase transformations in the matrix. In addition, microcrack formation and fracture of the carbide phase, which may lead to relaxation of local stresses in the real material, were not considered. Therefore, the calculated stress values should be regarded as model characteristics of the stress state, and the obtained results should primarily be considered as a basis for comparative analysis of the DXF-based and image-based FEM approaches, the influence of spatial discretization, and the representation of the carbide phase.

The developed approach can be used for further investigation of the effects of carbide-phase morphology, its volume fraction, and the structural state of the matrix on the local stress state of high-chromium cast irons. The ability to directly use binarized metallographic images provides a basis for comparative analysis of a large number of real microstructures without labor-intensive intermediate CAD geometry construction. Experimental verification of the absolute residual stress values using independent experimental methods, together with further improvement of the FEM model to account for internal stress relaxation associated with local plastic deformation, represents an important direction for further development of the proposed approach.

Conclusions

An image-based FEM approach was developed for the analysis of local thermal stresses in hypereutectic high-chromium cast irons directly from binarized metallographic images without intermediate CAD geometry construction.

It was demonstrated that image-based FEM models reproduce the main features of the stress distributions obtained using DXF-based models while substantially reducing the effort required for computational model preparation.

It was established that the influence of finite element size depends on the stress-state characteristic considered. The mean SP1 values change only slightly when the maximum element size of the image-based model is reduced from 0.5 to 0.2 μm, whereas P95 SP1 is more sensitive to spatial discretization and approaches the results of DXF-based modeling with mesh refinement.

It was shown that the representation and morphology of the carbide phase have a significant influence on stress localization in the carbide-matrix system, while the highest local stress values are sensitive to the method used to represent the phase boundaries.

Conflicts of interest. On behalf of all authors, the corresponding author states that there is no conflict of interest.

CRediT author statement: **V. Perezhogin**: Methodology, Calculations, Results summary, Article preparation; **A. Panichkin**: Article concept, Results discussion, Article editing; **G. Małgorzata**: Discussion and interpretation of scientific results, Provision of scientific and methodological recommendations for the manuscript; **S. Abyl**: literature review, Article design, Reviewing and Editing.

Acknowledgements. This research is funded by the Science Committee of the Ministry of Science and Higher Education of the Republic of Kazakhstan (Grant No. AP26102933).

Cite this article as: Perezhogin VYu, Panichkin AV, Małgorzata RG, Abyl SS. Image-Based FEM Modeling of the Stress State in Hypereutectic High-Chromium Cast Irons. Kompleksnoe Ispolzovanie Mineralnogo Syra = Complex Use of Mineral Resources. 2028; 346(3):131-141. https://doi.org/10.31643/2028/6445.33

Жоғары хромды гиперэвтектикалық шойындардағы кернеу күйін Image-based FEM-модельдеуі

[1] Пережогин В.Ю., [1]Паничкин А.В., [2]Małgorzata R.G., [1]Абыл С.С.

[1] Металлургия және кен байыту институты АҚ, Сәтбаев университеті, Алматы, Қазақстан
[2]Вроцлав ғылым және технология университеті, Вроцлав, Польша

Мақала келді: *17 маусым 2026*
Сараптамадан өтті: *26 шілде 2026*
Қабылданды: *8 қыркүйек 2026*

ТҮЙІНДЕМЕ
Нақты металлографиялық кескіндерге негізделген image-based шекті элементтік модельдеуді қолдана отырып, жоғары хромды гиперэвтектикалық шойындардағы жергілікті термиялық кернеулерді талдауға арналған тәсіл әзірленді. Есептік модельдерді дайындау Оцу әдісін қолдана отырып микроқұрылымды бинаризациялауды, шулы әсері бар объектілерді сүзгіден өткізуді және CAD автоматтандырылған жобалау жүйелерінде аралық геометрия құрусыз бинарланған кескін бойынша фазалардың кеңістіктік таралуын тікелей беруді қамтыды. Ұсынылған тәсілді верификациялау үшін Drawing Exchange Format (DXF) және бірдей микроструктуралық деректер негізінде құрылған image-based FEM-модельдер салыстырылды, сондай-ақ ақырғы элементтің өлшемінің есептелген кернеулік күйге әсері зерттелді. Көрсетілгендей, соңғы элемент тердің өлшемін біртіндеп азайтқан кезде image-based модельдеу нәтижелері, фазааралық шекаралардың дискретті пиксельдік бейнеленуіне қарамастан, DXF-based модельдердің нәтижелеріне сәйкес келетіні көрсетілді. Image-based тәсіл DXF-based модельдерді пайдалану арқылы алынған жергілікті кернеулердің таралуының негізгі заңдылықтарын қайталайды және бұл ретте кескінді векторизациялауды және аралық CAD/DXF-геометриясын құруды талап етпейді, бұл нақты микроқұрылымдардың есептеу модельдерін дайындауды айтарлықтай жеңілдетеді. Алынған нәтижелер жоғары хромды шойындардың күрделі көпфазалы микроқұрылымдарында термиялық кернеулердің локальды таралуын салыстырмалы талдау үшін image-based FEM модельдеуді қолдану мүмкіндігін растайды.

Түйін сөздер: жоғары хромды гиперэвтектикалық шойын, Image-based FEM, термиялық кернеулер, M_7C_3 карбидтері, микроқұрылымды талдау, ақырлы элементтерді модельдеу.

Авторлар туралы ақпарат:

Пережогин Виталий Юрьевич — *PhD, Материалтану зертханасының ғылыми қызметкері, Металлургия және кен байыту институты АҚ, Сәтбаев университеті, 050010, Шевченко көш., 29/133, Алматы, Қазақстан. E-mail: v.perezhogin@satbayev.university; ORCID ID: https://orcid.org/0009-0006-7881-4786*

Паничкин Александр Владимирович — *Техника ғылымдарының кандидаты, Материалтану зертханасының жетекші ғылыми қызметкері, Металлургия және кен байыту институты АҚ, Сәтбаев университеті, 050010, Шевченко көш., 29/133, Алматы, Қазақстан. Email: a.panichkin@satbayev.university; ORCID ID: https://orcid.org/0000-0002-2403-8949*

Małgorzata Rutkowska-Gorczyca — *PhD, Инженерия ғылымдарының докторы, Механика кафедрасы, Вроцлав ғылым және технология университеті, Вроцлав, 50-370, Польша. E-mail: Malgorzata.Rutkowska-Gorczyca@pwr.wroc.pl; ORCID ID: https://orcid.org/0000-0003-2712-5914*

Абыл Салима Серикқызы — *Докторант, Материалтану зертханасының ғылыми қызметкері, Металлургия және кен байыту институты АҚ, Сәтбаев университеті, 050010, Шевченко көш., 29/133, Алматы, Қазақстан. E-mail: Abyl.S@stud.satbayev.university; ORCID ID: https://orcid.org/0009-0006-1904-3483*

Image-based FEM-моделирование напряжённого состояния в высокохромистых заэвтектических чугунах

[1]Пережогин В.Ю., [1]Паничкин А.В., [2]Małgorzata R.G., [1]Абыл С.С.

[1] АО Институт металлургии и обогащения, Satbayev University, Алматы, Казахстан
[2] Вроцлавский университет науки и техники, Вроцлав, Польша

Поступила: *17 июня 2026*
Рецензирование: *26 июля 2026*
Принята в печать: *8 сентября 2026*

АННОТАЦИЯ

Разработан подход к анализу локальных термических напряжений в высокохромистых заэвтектических чугунах с использованием image-based конечно-элементного моделирования на основе реальных металлографических изображений. Подготовка расчётных моделей включала бинаризацию микроструктуры методом Оцу, фильтрацию шумовых объектов и непосредственное задание пространственного распределения фаз по бинаризованному изображению без промежуточного построения геометрии в системах автоматизированного проектирования (CAD). Для верификации предложенного подхода выполнено сопоставление Drawing Exchange Format (DXF) и image-based FEM-моделей, построенных на основе одинаковых микроструктурных данных, а также исследовано влияние размера конечного элемента на рассчитанное напряжённое состояние. Показано, что при последовательном уменьшении размера конечных элементов результаты image-based моделирования приближаются к результатам DXF-based моделей, несмотря на дискретное пиксельное представление межфазных границ. Image-based подход воспроизводит основные закономерности локального распределения напряжений, полученные с использованием DXF-based моделей, и при этом не требует векторизации изображения и построения промежуточной CAD/DXF-геометрии, что существенно упрощает подготовку расчётных моделей реальных микроструктур. Полученные результаты подтверждают возможность применения image-based FEM-моделирования для сравнительного анализа локального распределения термических напряжений в сложных многофазных микроструктурах высокохромистых чугунов.

Ключевые слова: высокохромистый заэвтектический чугун, image-based FEM, термические напряжения, карбиды M_7C_3, анализ микроструктуры, конечно-элементное моделирование.

Информация об авторах:

Пережогин Виталий Юрьевич — *PhD, научный сотрудник, Лаборатория металловедения, АО Институт металлургии и обогащения, Satbayev University, 050010, ул. Шевченко, 29/133, Алматы, Казахстан. E-mail: v.perezhogin@satbayev.university; ORCID ID: https://orcid.org/0009-0006-7881-4786*

Паничкин Александр Владимирович — *Кандидат технических наук, старший научный сотрудник, Лаборатория металловедения, АО Институт металлургии и обогащения, Satbayev University, 050010, ул. Шевченко, 29/133, Алматы, Казахстан. Email: a.panichkin@satbayev.university; ORCID ID: https://orcid.org/0000-0002-2403-8949*

Małgorzata Rutkowska-Gorczyca — *Кандидат наук, Доктор технических наук, Кафедра механики, Вроцлавский университет науки и техники, 50-370 Вроцлав, Польша. E-mail: Malgorzata.Rutkowska-Gorczyca@pwr.wroc.pl; ORCID ID: https://orcid.org/0000-0003-2712-5914*

Абыл Салима Серикқызы — *Докторант, младший научный сотрудник, Лаборатория металловедения, АО Институт металлургии и обогащения, Satbayev University, 050010, ул. Шевченко, 29/133, Алматы, Казахстан. E-mail: Abyl.S@stud.satbayev.university; ORCID ID: https://orcid.org/0009-0006-1904-3483*

References

[1] Karantzalis E, Lekatou A, Mavros H. Microstructure and properties of high chromium cast irons: effect of heat treatments and alloying additions. International Journal of Cast Metals Research. 2009; 22(6):448-456. https://doi.org/10.1179/174313309X436637

[2] Coronado J.J. Effect of $(Fe,Cr)_7C_3$ carbide orientation on abrasion wear resistance and fracture toughness. Wear. 2011; 270(3-4):287-293. https://doi.org/10.1016/j.wear.2010.10.070

[3] Jokari-Sheshdeh M, Ali Y, Gallo SC, Lin W, Gates JD. Effect of Cr: Fe ratio on the mechanical properties of $(Cr, Fe)_7C_3$ ternary carbides in abrasion-resistant white cast irons. Journal of Materials Science. 2023; 58:7504-7521. https://doi.org/10.1007/s10853-023-08461-z

[4] Wiengmoon A. Carbides in high chromium cast irons. Naresuan University Engineering Journal. 2011; 6(1):64-71. https://doi.org/10.14456/nuej.2011.6

[5] Li Y, Gu L, Du M, et al. Microstructure and properties of hypereutectic high chromium cast iron containing nitrogen. Materials Science and Technology. 2024; 40(1):26-41. https://doi.org/10.1177/02670836231212611

[6] Panichkin AV, Korotenko RY, Kenzhegulov AK, et al. Porosity and non-metallic inclusions in cast iron produced with a high proportion of scrap. Kompleksnoe Ispolzovanie Mineralnogo Syra = Complex Use of Mineral Resources. 2022; 323(4):68–76. https://doi.org/10.31643/2022/6445.42

[7] Panichkin A, Uskenbayeva A, Kenzhegulov A, Mamaeva A, Imbarova A, Kshibekova B, Alibekov Zh, Nurhadiyanto D, Yunita I. Assessment of the effect of small additions of some rare earth elements on the structure and mechanical properties of castings from hypereutectic chromium white irons. AIMS Materials Science. 2023; 10(3):517–540. https://doi.org/10.3934/matersci.2023029

[8] Panichkin AV, Wieleba WK, Uskenbayeva AM, Kenzhegulov AK, Mamayeva AA, Kvyatkovskii SA, Kasenova BA, Imbarova AT. Effect of thermal treatment of chromium iron melts on the structure and properties of castings. Materials Research Express. 2023; 10:086502. https://doi.org/10.1088/2053-1591/acead7

[9] Panichkin AV, Mamaeva AA, Kenzhegulov AK, Kshibekova BB, Uskenbaeva AM, Imbarova AT. The influence of cooling rate on the structure and properties of castings of hypereutectic high-chromium cast iron when they are modified with B, Bi, Sb, Sn, Ca. AIMS Materials Science. 2024; 11(1):58–80. https://doi.org/10.3934/matersci.2024003

[10] Panichkin AV, Mamaeva AA, Kenzhegulov AK, Kshibekova BB, Uskenbaeva AM, Imbarova AT, Alibekov Zh. Effect of carbon and cooling rate on the structure of hypereutectic high chromium cast iron in the cast state and after heat treatment. Journal of Composites Science. 2023; 7(12):483. https://doi.org/10.3390/jcs7120483

[11] Albertin E, Sinatora A. Effect of carbide fraction and matrix microstructure on the wear of cast iron balls tested in a laboratory ball mill. Wear. 2001; 250:492-501. https://doi.org/10.1016/S0043-1648(01)00664-0

[12] Wang J, Liu T, Xing X, Li J, Qi X, Yang Q. Study of the wear resistance of hypereutectic Fe-Cr-C hardfacing alloy reinforced with carbide particles. Materials Research Express. 2022; 9:106507. https://doi.org/10.1088/2053-1591/ac94b6

[13] Evans LM, Sözümert E, Keenan BE, et al. A Review of Image-Based Simulation Applications in High-Value Manufacturing. Archives of Computational Methods in Engineering. 2023; 30:1495-1552. https://doi.org/10.1007/s11831-022-09836-2

[14] Reid A, Langer S, Lua RC, et al. Image-based finite element mesh construction for material microstructures. Computational Materials Science. 2008; 43(4):989-999. https://doi.org/10.1016/j.commatsci.2008.02.016

[15] Golt MC, Hernández-Rivera E. An Automated Workflow for Meshing Evolving Microstructures from High-Throughput Grain Growth Simulations. Proceedings of the COMSOL Conference, Boston, USA. 2018.

[16] Gu D, He B. Finite Element Simulation and Experimental Investigation of Residual Stresses in Selective Laser Melted Ti-Ni Shape Memory Alloy. Computational Materials Science. 2016; 117:221-232. https://doi.org/10.1016/j.commatsci.2016.01.044

[17] Li Y, Zhou K, Tan P, Tor SB, Chua CK, Leong KF. Modelling temperature and residual stress fields in selective laser melting. International Journal of Mechanical Sciences. 2018; 136:24-35. https://doi.org/10.1016/j.ijmecsci.2017.12.001

[18] Schneider CA, Rasband WS, Eliceiri KW. NIH Image to ImageJ: 25 Years of Image Analysis. Nature Methods. 2012; 9:671-675. https://doi.org/10.1038/nmeth.2089

[19] Otsu N. A Threshold Selection Method from Gray-Level Histograms. IEEE Transactions on Systems, Man, and Cybernetics. 1979; 9:62-66. https://doi.org/10.1109/TSMC.1979.4310076

[20] Gonzalez RC, Woods RE. Digital Image Processing. 4th ed. Pearson Education. 2018, 1022.

[21] Raghavan V. C-Cr-Fe (Carbon-Chromium-Iron). Journal of Phase Equilibria. 2002; 23:513–514. https://doi.org/10.1361/105497102770331226

[22] Khvan AV, Hallstedt B, Broeckmann C. A thermodynamic evaluation of the Fe–Cr–C system. CALPHAD: Computer Coupling of Phase Diagrams and Thermochemistry. 2014; 46:24-33. https://doi.org/10.1016/j.calphad.2014.01.002

[23] Maldonado-Ruiz SI, et al. Effect of V-Ti on the Microstructure and Abrasive Wear Behavior of 6CrC Cast Steel Mill Balls. Journal of Minerals and Materials Characterization and Engineering. 2014; 2:383-391. http://dx.doi.org/10.4236/jmmce.2014.25043

[24] Richter F. The Physical Properties of Steels: The 100 Steels Programme. Part I: Tables and Figures. Mülheim an der Ruhr, Germany. https://www.tugraz.at/fileadmin/user_upload/Institute/IEP/Thermophysics_Group/Files/Staehle-Richter.pdf

[25] Xiao B, Xing JD, Feng J, Li YF, Zhou CT, Su W, Xie XJ, Chen YH. Theoretical study on the stability and mechanical property of Cr_7C_3. Physica B. 2008; 403(13-16):2273–2281. https://doi.org/10.1016/j.physb.2007.12.012

[26] Sun L, Ji X, Zhao L, Zhai W, Xu L, Dong H, Liu Y, Peng J. First Principles Investigation of Binary Chromium Carbides Cr_7C_3, Cr_3C_2 and $Cr_{23}C_6$: Electronic Structures, Mechanical Properties and Thermodynamic Properties under Pressure. Materials. 2022; 15(2):558. https://doi.org/10.3390/ma15020558

[27] COMSOL Multiphysics® v. 6.1. Reference Manual. COMSOL AB, Stockholm, Sweden. 2022.

[28] Wang J, Xing X, Zhou Y, et al. Formation mechanism of ultrafine M_7C_3 carbide in a hypereutectic Fe-25Cr-4C-0.5Ti-0.5Nb-0.2N-2LaAlO3 hardfacing alloy layer. Journal of Materials Research and Technology. 2020; 9(4):7711-7720. https://doi.org/10.1016/j.jmrt.2020.05.039